

# Escaping the Hydrolysis Trap: An Agentic Workflow for Inverse Design of Durable Photocatalytic Covalent Organic Frameworks

Iman Peivaste<sup>1,2,\*</sup>, Nicolas D. Boscher<sup>1</sup>, Ahmed Makradi<sup>1</sup>, Salim Belouettar<sup>1</sup>

<sup>1</sup> Luxembourg Institute of Science and Technology (LIST), 5, Avenue des Hauts-Fourneaux, Esch-sur-Alzette, 4362, Luxembourg

<sup>2</sup> Department of Physics and Materials Science, University of Luxembourg, L-4365 Esch-sur-Alzette, Luxembourg

\*Corresponding Author: iman.peivaste@list.lu

March 6, 2026

## Abstract

Covalent organic frameworks (COFs) are promising photocatalysts for solar hydrogen production, yet the most electronically favorable linkages, imines, hydrolyze rapidly in water, creating a stability–activity trade-off that limits practical deployment. Navigating the combinatorial design space of nodes, linkers, linkages, and functional groups to identify candidates that are simultaneously active and durable remains a formidable challenge. Here we introduce **Ara**, a large-language-model (LLM) agent that leverages pretrained chemical knowledge, donor–acceptor theory, conjugation effects, and linkage stability hierarchies, to guide the search for photocatalytic COFs satisfying joint band-gap, band-edge, and hydrolytic-stability criteria. Evaluated against random search and Bayesian optimization (BO) over a space consisting of candidates with various nodes, linkers, linkages, and r-groups, screened with a GFN1-xTB fragment pipeline, Ara achieves a 52.7% hit rate ( $11.5\times$  random,  $p = 0.006$ ), finds its first hit at iteration 12 versus 25 for random search, and significantly outperforms BO ( $p = 0.006$ ). Inspection of the agent’s reasoning traces reveal interpretable chemical logic: early convergence on vinylene and  $\beta$ -ketoenamine linkages for stability, node selection informed by electron-withdrawing character, and systematic R-group optimization to center the band gap at 2.0 eV. Exhaustive evaluation of the full search space uncovers a complementary exploitation-exploration trade-off between the agent and BO, suggesting that hybrid strategies may combine the strengths of both approaches. These results demonstrate that LLM chemical priors can substantially accelerate multi-criteria materials discovery.

## Introduction

Photocatalytic water splitting driven by solar energy offers a sustainable route to hydrogen fuel, and the search for efficient, stable photocatalysts remains one of the central challenges in materials science [1, 2, 3, 4]. Covalent organic frameworks (COFs), crystalline, porous polymers assembled from organic building blocks through reversible covalent bonds, have emerged as attractive photocatalyst candidates owing to their tunable band gaps, high surface areas, and modular synthetic chemistry [5, 6, 7]. In principle, the band gap and conduction-band minimum (CBM) of a COF can be rationally engineered by selecting appropriate electron-donating and

electron-withdrawing building blocks, making COFs a natural platform for inverse design [8, 9]. In practice, however, a fundamental tension exists between electronic performance and chemical durability: the imine (C=N) linkages that dominate the COF literature are susceptible to hydrolysis under the aqueous, often acidic conditions of photocatalytic operation [10, 11]. This "hydrolysis trap" means that many COFs with promising band gaps degrade before they can function.

The design space for COF photocatalysts is vast. Combining a modest library of seven trigonal nodes, nineteen ditopic linkers, four linkage chemistries, and ten aromatic R-group substituents yields 820 compatibility-constrained candidates, and realistic libraries can be orders of magnitude larger [12]. Density functional theory (DFT) calculations, while accurate, require hours per candidate for periodic structures, making exhaustive screening prohibitively expensive [13, 14]. Even semiempirical methods such as the GFN*n*-xTB family [15] require minutes per geometry optimization, and the multi-criteria nature of the problem, simultaneous satisfaction of band-gap, band-edge, and stability requirements, rules out simple ranking on a single descriptor.

Several computational strategies have been proposed to navigate large materials design spaces. High-throughput virtual screening enumerates and evaluates candidates sequentially but scales poorly beyond a few hundred evaluations [16]. Bayesian optimization (BO) places a Gaussian process surrogate over molecular fingerprints and uses an acquisition function to balance exploration and exploitation [17, 18]; however, BO treats molecules as feature vectors and cannot reason about categorical chemical concepts such as linkage hydrolysis or band-gap tuning via donor-acceptor engineering. Machine-learning surrogate models accelerate screening once trained [19, 20, 21, 22] but face a cold-start problem when no labelled data exist for a new materials class or property combination.

Large language models (LLMs) offer a qualitatively different approach. Trained on the scientific literature, LLMs encode chemical knowledge, donor-acceptor theory, and conjugation effects, functional-group reactivity that can serve as a prior for materials design without task-specific training data [23, 24, 25]. Recent work has explored LLMs as assistants for retrosynthesis [26], molecular property prediction [27], deriving design rules [28], and reaction optimization [29], but their application to multi-criteria materials discovery with explicit chemical reasoning remains largely unexplored. Here we present **Ara**, an LLM-guided agent built on Google’s Gemini model [30] that navigates COF design space using an iterative reasoning loop: at each step, the agent receives feedback on its previous selections (band gap, CBM, stability score) and proposes a new candidate with a brief chemical justification. We pair the agent with a fragment-based screening pipeline that uses GFN1-xTB to compute vertical ionization potentials and electron affinities, calibrated against periodic DFT band gaps for 13 COFs (Spearman  $\rho = 0.71$ ,  $p = 0.006$ ). A composite stability index ( $S_{\text{CSI}}$ ) that integrates linkage chemistry, steric shielding, and hydrophobicity encodes the stability axis of the design problem.

We evaluate Ara against random search and BO over 200 iterations across five independent seeds. The agent achieves a 52.7% hit rate, 11.5 times that of random search ( $p = 0.006$ , Mann-Whitney U, one-sided), and significantly outperforms BO ( $p = 0.006$ ) on cumulative hits. Analysis of the agent’s reasoning traces reveals interpretable chemical logic: convergence on non-hydrolyzable vinylene linkages, avoidance of excessively electron-withdrawing nodes, and systematic R-group tuning. Exhaustive evaluation of all candidates identifies 38 ground-truth hits, enabling an oracle analysis that exposes a complementary exploitation-exploration trade-off: the agent excels at rapidly identifying high-quality candidates within a budget-constrained campaign, while BO maps a larger fraction of the hit landscape through systematic exploration. Together, these results demonstrate that LLM chemical priors can substantially accelerate multi-criteria materials discovery and that agent-based and surrogate-based strategies serve complementary experimental goals.

# Results

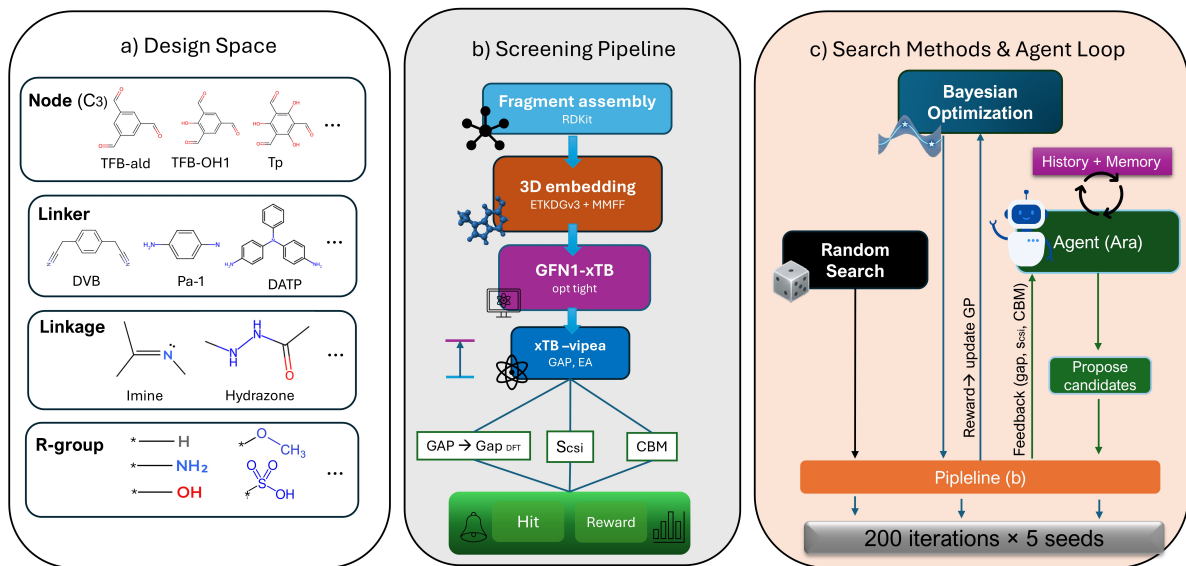


Figure 1: Overview of the Ara agentic workflow for COF photocatalyst discovery. (a) The combinatorial design space comprises 820 candidates formed from 7 trigonal nodes, 19 ditopic linkers, 4 linkage chemistries of varying hydrolytic stability, and 10 aromatic R-group substituents, subject to chemical compatibility constraints. (b) Each candidate is evaluated through a fragment-based screening pipeline: a node–linker–node repeat unit is assembled via RDKit, embedded in 3D, optimized with GFN1-xTB, and scored for band gap (IP–EA, mapped to the DFT scale via a calibrated transfer function), conduction-band minimum (CBM), and composite stability index (S\_CSI). A candidate is classified as a hit if it satisfies all three criteria simultaneously. (c) Three search strategies are compared: random sampling, Bayesian optimization with a Gaussian process surrogate on Morgan fingerprints, and the Ara LLM agent, which iteratively proposes candidates with explicit chemical reasoning, receives quantitative feedback, and refines its selections over 200 iterations.

## Calibration validates fragment-based screening

The fragment-based fundamental gap (IP–EA) from GFN1-xTB correlated significantly with periodic DFT band gaps across six linkage types (Spearman  $\rho = 0.71$ ,  $p = 0.006$ ,  $n = 13$ ; Supplementary Table S2), validating the screening pipeline for comparative ranking of candidates (Fig. 2). Three methodological pivots were required to reach this result. First, initial attempts using  $2 \times 2$  periodic clusters inverted the gap ranking of known COFs, motivating a switch to repeat-unit fragments ( $\sim 50$ – $80$  atoms) that preserved the correct ordering [31]. Second, HOMO–LUMO gaps from xTB Single-point calculations showed no correlation with DFT values ( $\rho = -0.18$ ,  $p = 0.70$  for a seven-COF imine-only subset), whereas fundamental gaps computed as IP–EA via the delta-SCF protocol (xtb --vipea) [15] recovered the expected trend, a finding consistent with the known inadequacy of Kohn-Sham eigenvalue differences for organic framework quasiparticle gaps. Third, five  $\beta$ -ketoenamine COFs were excluded from calibration because their fragment SMILES encoded the imine tautomeric form rather than the correct

keto-enamine structure, producing erroneous electronic structures. A linear transfer function,

$$\text{gap}_{\text{DFT}} \approx 0.65 \times \text{gap}_{\text{xTB}} - 0.70 \quad (R^2 = 0.62), \quad (1)$$

mapped xTB fundamental gaps onto the DFT scale for downstream screening.

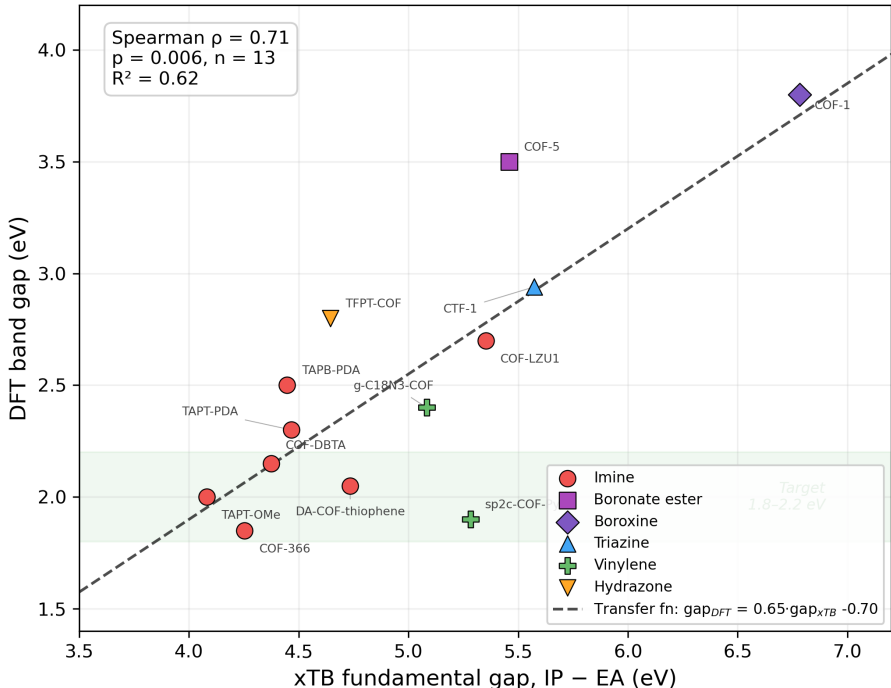


Figure 2: Scatter plot of xTB (IP-EA) fundamental gap versus DFT band gap for 13 COFs spanning six linkage types, with the linear transfer function overlaid. The calibration set includes boronate ester, boroxine, and triazine linkage types not present in the search space to broaden the range of the transfer function. Note that CTF-1 employs triazine ring formation as the linkage chemistry, distinct from triazine-containing nodes (e.g., TFPT-ald, TAPT) that connect via imine or other bond types.

These results establish that fragment-level IP-EA calculations from GFN1-xTB provide a computationally inexpensive yet reliable proxy for periodic DFT band gaps. The transfer function and CBM calibration (see Methods) formed the quantitative backbone of all subsequent screening.

### Agent achieves superior sample efficiency

We compared three search methods, random search, Bayesian optimization (BO), and Ara (LLM agent), over 200 iterations with five independent random seeds each. A candidate was classified as a “hit” if it simultaneously satisfied three criteria: a corrected band gap between 1.8 and 2.2 eV, CBM below 0 V, and composite stability index  $S_{\text{CSI}} \geq 0.7$  (see Methods). Table 1 summarizes the results.

Table 1: Comparative study results (mean  $\pm$  s.d. over five seeds).

Method	Cum. hits	Hit rate (%)	First hit (iter.)	Best reward	Success rate (%)
Random	9.2 $\pm$ 1.9	4.6	25 $\pm$ 16	0.903 $\pm$ 0.012	82.1
BO	28.2 $\pm$ 3.8	14.1	22 $\pm$ 31	0.921 $\pm$ 0.000	100.0
Agent	105.4 $\pm$ 40.9	52.7	12 $\pm$ 13	0.895 $\pm$ 0.016	95.7

The Ara agent discovered hits at 11.5 times the rate of random search ( $p = 0.006$ , Mann–Whitney U, one-sided), with the earliest median first-hit iteration among all methods (iteration 12 versus 25 for random and 22 for BO; Table 1, Fig. 3). The cumulative hit curves (Fig. 3) show that the agent’s advantage is not a transient early effect: the agent curve rises steeply from approximately iteration 15 and continues to dominate both baselines through iteration 200. The agent also significantly outperformed BO on cumulative hits ( $U = 25$ ,  $p = 0.006$ ). BO, however, achieved the highest single-candidate reward (0.921), reflecting its strength at scalar optimization through Gaussian process extrapolation, whereas the agent’s advantage lay in the sustained identification of candidates meeting all three hit criteria simultaneously.

Despite 23% of agent iterations falling back to random selection due to model-output parsing failures, the agent achieved an 11.5-fold improvement over pure random search. This implies that the  $\approx 77\%$  of successfully guided iterations were dramatically more effective than chance, and that even partial LLM guidance provides substantial benefit. The xTB evaluation success rate was 95.7% for agent-selected candidates versus 82.1% for random, suggesting that the agent’s chemistry-aware selections also avoided combinations prone to assembly or convergence failure.

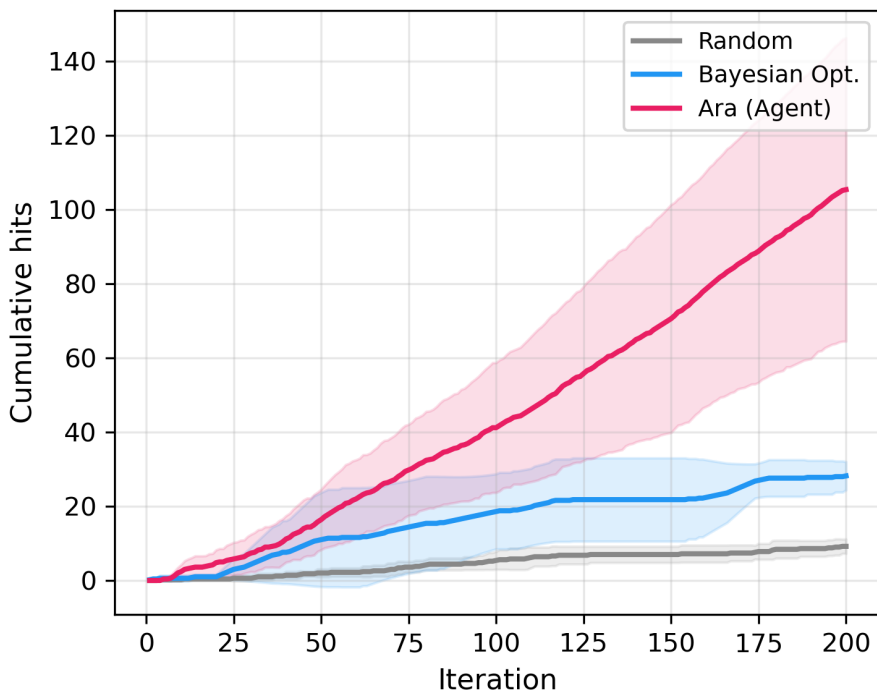


Figure 3: Cumulative hits versus iteration for random search (grey), Bayesian optimization (blue), and Ara (agent, pink). Shaded regions indicate mean  $\pm$  s.d. across five random seeds (200 iterations per run). A hit is defined as a candidate satisfying 1.8–2.2 eV band gap,  $CBM < 0$  V, and  $S_{CSI} \geq 0.7$ . The agent outperforms both random search and BO in cumulative hits and discovers its first hit sooner.

Table 2: Selected reasoning traces from the agent (20-iteration dedicated run, seed 42). “Hit” column marks candidates meeting all three criteria.

Iter.	Selection	Gap (eV)	$S_{CSI}$	Hit	Reasoning (abbreviated)
0	Tp + BD + $\beta$ -keto. + H	2.61	0.67	—	$\beta$ -Ketoenamine for stability via irreversible tautomerization.
1	Tp + BTDA + $\beta$ -keto. + H	2.50	0.64	—	Benzothiadiazole acceptor to narrow the gap into the target range.
2	TFPT-ald + DVB + vinyl. + H	1.53	0.73	—	Triazine acceptor + vinylene for non-hydrolysable stability; gap too low.
3	TFB + DVB + vinyl. + H	2.13	0.73	<b>Hit</b>	Electron-neutral TFB replaces strong acceptor TFPT-ald to widen the gap.
4	TFP-OH1 + DVB + vinyl. + H	2.11	0.73	<b>Hit</b>	Mild $e^-$ -donor OH narrows the gap slightly from 2.13 toward 2.0 eV.
5	TFP-OH1 + DVB + vinyl. + OMe	2.02	0.75	<b>Hit</b>	Methoxy donor narrows the gap toward the 2.0 eV ideal.
8	TFB + DVB + vinyl. + OMe	2.03	0.73	<b>Hit</b>	Same strategy applied to TFB scaffold; gap centres at 2.0 eV.
11	TFB + DVB + vinyl. + Me	2.12	0.73	<b>Hit</b>	Weak donor; gap remains in target window.

The agent’s decisive advantage in cumulative hits, combined with earlier first-hit discovery, establishes that LLM-guided search substantially outperforms both random and surrogate-based strategies for this multi-criteria design task.

## Chemical reasoning drives agent performance

To understand why the agent outperforms BO, we collected detailed reasoning traces from a dedicated 20-iteration run with increased output-token limits (see Methods). The traces reveal a coherent chemical strategy that unfolds over the first dozen iterations (Table 2).

The reasoning traces reveal that the agent’s selections were guided by explicit chemical logic, band-gap tuning via donor–acceptor engineering, linkage stability hierarchies, and iterative refinement based on quantitative feedback, rather than pattern matching or memorization of training data. The agent began by testing  $\beta$ -ketoenamine linkages (iterations 0–1), explicitly citing their hydrolytic stability via irreversible tautomerization. Although these candidates had adequate stability indices, their band gaps exceeded the 2.2 eV upper bound. At iteration 2, the agent switched to a vinylene linkage with the strongly electron-withdrawing TFPT-ald node, reasoning that the donor–acceptor combination would narrow the gap while providing non-hydrolysable C=C bonds. When the resulting gap (1.53 eV) fell below the 1.8 eV threshold, the agent corrected course at iteration 3 by replacing TFPT-ald with the electron-neutral TFB node, a move it justified as reducing excessive acceptor character, widening the gap to 2.13 eV and producing the first hit.

From iteration 4 onward, the agent pursued a systematic optimization strategy within the vinylene-linked scaffold family. It first tested TFP-OH1, a node with a mild electron-donating hydroxyl group, observing that the gap narrowed slightly (2.11 eV). It then explored R-group substitutions, OMe (gap 2.02 eV),  $NH_2$  (2.10 eV), OH (2.14 eV), Me (2.12 eV), using donor and acceptor electronic effects to fine-tune the gap toward the 2.0 eV optimum. Each selection was accompanied by a reasoning statement that referenced the previous result and predicted the direction of the gap change, and these predictions were frequently correct. This iterative refinement loop, propose, evaluate, reason, adjust, is a qualitatively different mode of search from either random sampling or fingerprint-based acquisition functions.

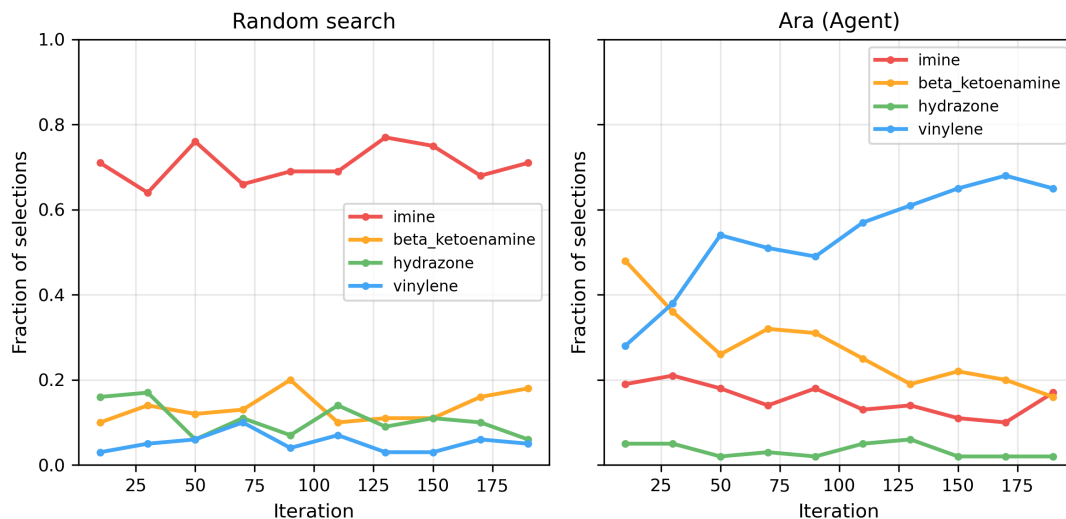


Figure 4: Linkage-type distribution over search iterations. Fraction of candidate selections belonging to each linkage type (imine,  $\beta$ -ketoenamine, hydrazone, vinylene) in a rolling window of 20 iterations, averaged over five seeds. Left: random search maintains a roughly uniform distribution across linkage types throughout the run. Right: Ara (agent) shifts from a mixed distribution early in the search to a strong preference for vinylene and, to a lesser extent,  $\beta$ -ketoenamine by iteration 50, reflecting chemistry-aware prioritization of hydrolytically stable linkages (high  $S_{\text{CSI}}$ ) while exploring node and R-group choices to meet the band-gap and band-edge criteria.

Analysis of the linkage-type distribution over the full 200-iteration runs confirms the pattern quantitatively (Fig. 4): the agent shifts from a mixed distribution early on to an overwhelming preference for vinylene linkages (and, to a lesser extent,  $\beta$ -ketoenamine) by iteration 50, whereas random search maintains a uniform distribution throughout. The agent’s three-level strategy, prioritise hydrolytically stable linkages, select electronically appropriate nodes, then tune the band gap through R-group substitution, mirrors the hierarchical reasoning a human chemist would apply and is not naturally accessible to fingerprint-based BO without explicit categorical features for linkage chemistry.

## Search space characterization and exploitation-exploration trade-off

Exhaustive evaluation of all 820 candidates yielded 670 successful computations and identified 38 ground-truth hits, a global hit rate of 5.7% (see Methods). The hits were concentrated in two linkage families: 30 vinylene-linked (79%) and 8  $\beta$ -ketoenamine-linked (21%) COFs, with no imine- or hydrazone-linked candidates meeting all three criteria simultaneously (Supplementary Table S3). The concentration of hits in these two families reflects the fundamental stability-activity trade-off: only vinylene and  $\beta$ -ketoenamine linkages achieve  $S_{\text{CSI}} \geq 0.7$  while maintaining band gaps in the 1.8–2.2 eV window. Within the vinylene family, hit rates varied strongly by node: TFB and TFP-OH1 produced hits across nearly all R-groups, Tp was partially successful (9 of 10 R-groups, missing only  $\text{SO}_3\text{H}$ ), and TFPT-ald yielded only a single hit ( $\text{CF}_3$ ), as its strongly electron-withdrawing triazine core pushed the band gap below 1.8 eV for all other substitutions.

Using this ground truth, we computed oracle recovery, the fraction of the 38 unique hits discovered at least once, for each method (Supplementary Fig. S2). BO achieved substantially higher

oracle coverage than the agent, driven by the Gaussian process uncertainty term that actively pushes exploration into unsampled regions of fingerprint space. The agent’s lower oracle recovery reflects its strong exploitation of a small number of productive vinylene-linked scaffolds: once it identified TFB + DVB + vinylene as a reliable hit source, it focused on R-group variants rather than exploring distant chemical families. Random search provided baseline diversity intermediate between the two. This exploitation-exploration trade-off has a practical interpretation: in a budget-constrained experimental campaign where each evaluation corresponds to a DFT calculation or laboratory synthesis, the agent’s 53% per-iteration success rate is decisive; in a program seeking comprehensive characterization of the full design space, BO’s systematic exploration is preferable. These are complementary, not competing, strengths.

### Agent advantage is robust to scoring-function weights

The composite stability index  $S_{\text{CSI}}$  combines linkage stability ( $S_{\text{linkage}}$ ), steric shielding ( $S_{\text{shielding}}$ ), and hydrophobicity ( $S_{\text{hydrophobicity}}$ ) with weights 0.50, 0.30, and 0.20, respectively. To assess whether the agent’s advantage depends on this specific weight choice, we performed a sensitivity analysis across 30 weight triples in which the linkage weight varied from 0.3 to 0.7 and the remaining weight was distributed between shielding and hydrophobicity in increments of 0.1 (Supplementary Fig. S1). For all 21 weight combinations where the search space contained at least 10 hits, the regime in which the comparison is statistically meaningful, the agent-to-random hit ratio ranged from  $2.5\times$  to  $14.3\times$ , consistently exceeding the  $2\times$  threshold. The nine excluded triples had extreme shielding weights ( $\geq 0.4$ ) that reduced the number of hits in the space to fewer than three, rendering ratio comparisons uninformative.

The robustness of the agent advantage across weight triples arises because the agent’s primary learned strategy, preferring vinylene and  $\beta$ -ketoenamine linkages, produces high  $S_{\text{linkage}}$  scores regardless of the exact weight assigned to this component. Stated differently, the agent’s categorical reasoning about linkage chemistry is orthogonal to the specific numerical weighting within  $S_{\text{CSI}}$ , making the comparative result insensitive to this methodological choice.

## Discussion

This work demonstrates that pretrained large language models encode chemical knowledge sufficient to guide efficient navigation of a multi-criteria COF design space. The Ara agent achieved a hit rate 11.5 times that of random search ( $p < 0.01$ ), with the fastest convergence to the first hit among all tested methods (Table 1). Sensitivity analysis across 30  $S_{\text{CSI}}$  weight combinations confirmed that this advantage persists throughout the plausible weight space (Supplementary Fig. S1), ruling out dependence on the specific scoring-function parameterization. These results establish that LLM chemical priors, specifically donor-acceptor theory, linkage stability knowledge, and structure-property reasoning, provide a viable foundation for materials discovery agents.

The agent’s performance can be traced to specific chemical reasoning strategies that are visible in its output and verifiable against chemical intuition. First, the agent rapidly converged on non-hydrolyzable vinylene (C=C) linkages, recognizing, without being told, that the absence of a hydrolyzable bond provides the highest achievable stability score. Second, the agent learned to avoid the strongly electron-withdrawing TFPT-ald node, correctly reasoning that the resulting donor-acceptor mismatch pushes the band gap below the 1.8 eV threshold; this mirrors the node dependence observed in the exhaustive evaluation, where TFPT-ald + DVB + vinylene produced only one hit out of ten R-groups. Third, the agent systematically explored R-group substitutions,

OMe, NH<sub>2</sub>, OH, Me, tBu, to fine-tune the band gap toward the 2.0 eV optimum. This three-level strategy (linkage → node → R-group) was discovered from evaluation feedback alone and mirrors the hierarchical reasoning a human chemist would apply. It is not naturally accessible to methods that encode molecules solely as numerical fingerprints without explicit categorical features for linkage chemistry. The agent was not, however, infallible: it occasionally proposed imine-linked candidates in early iterations despite their low  $S_{\text{linkage}}$  scores (8 imine attempts in the first 50 iterations of seed 42, none yielding hits), and it revisited the TFPT-ald node a second time at iteration 13 despite its earlier failure (gap 1.75 eV, still below threshold). These episodes, together with the 23% parse-failure rate, indicate that current LLMs remain imperfect chemical reasoners, though the overall strategy was sound. The agent’s performance can be traced to specific chemical reasoning strategies that are visible in its output and verifiable against chemical intuition. First, the agent rapidly converged on non-hydrolysable vinylene (C=C) linkages, recognizing, without being told, that the absence of a hydrolyzable bond provides the highest achievable stability score. Second, the agent learned to avoid the strongly electron-withdrawing TFPT-ald node, correctly reasoning that the resulting donor–acceptor mismatch pushes the band gap below the 1.8 eV threshold; this mirrors the node dependence observed in the exhaustive evaluation, where TFPT-ald + DVB + vinylene produced only one hit out of ten R-groups. Third, the agent systematically explored R-group substitutions, OMe, NH<sub>2</sub>, OH, Me, tBu, to fine-tune the band gap toward the 2.0 eV optimum. This three-level strategy (linkage → node → R-group) was discovered from evaluation feedback alone and mirrors the hierarchical reasoning a human chemist would apply. It is not naturally accessible to methods that encode molecules solely as numerical fingerprints without explicit categorical features for linkage chemistry. The agent was not, however, infallible: it occasionally proposed imine-linked candidates in early iterations despite their low  $S_{\text{linkage}}$  scores (8 imine attempts in the first 50 iterations of seed 42, none yielding hits), and it revisited the TFPT-ald node a second time at iteration 13 despite its earlier failure (gap 1.75 eV, still below threshold). These episodes, together with the 23% parse-failure rate, indicate that current LLMs remain imperfect chemical reasoners, though the overall strategy was sound.

Exhaustive evaluation of all 670 successfully computed candidates identified 38 ground-truth hits (Supplementary Table S3), enabling assessment of each method’s exploration breadth. The agent’s high per-iteration hit rate reflects strong exploitation of a small number of productive chemical families, primarily vinylene-linked COFs with TFB, TFP-OH1, and Tp nodes, rather than broad coverage of the full hit landscape. Bayesian optimization, driven by its Gaussian process uncertainty term and built-in deduplication, achieved substantially higher unique-hit coverage (Supplementary Fig. S2). These complementary behaviors suggest that budget-constrained experimental campaigns benefit from the agent’s rapid convergence to high-quality candidates, while programs seeking comprehensive characterization of the design space may prefer BO’s systematic exploration. Hybrid strategies, using the agent for rapid initial convergence and BO for subsequent diversification, represent a promising direction that could combine the strengths of both approaches.

Approximately 23% of agent iterations produced outputs that could not be parsed into valid candidate selections and were replaced with random draws. Rather than invalidating the comparison, this failure mode introduces a conservative bias: the agent effectively operated at approximately 77% agency, with nearly one quarter of its budget consumed by random sampling. That it nonetheless achieved an 11.5-fold improvement over pure random search implies that the guided iterations were dramatically more efficient than chance. Improving LLM instruction-following and output formatting, through fine-tuning, constrained decoding, or structured-output APIs, would further enhance performance.

Several limitations should be acknowledged. First, the study uses a single LLM (Gemini-3-flash-

preview); generalization across model families (e.g., GPT-5, Claude) and sizes remain to be established. Second, all evaluations are at the GFN1-xTB semiempirical level, while the transfer function provides a calibrated mapping to DFT band gaps (Spearman  $\rho = 0.71$ ), periodic DFT confirmation of the top agent-discovered candidates is a necessary next step. Third, the search space is pre-enumerated (820 candidates); in open-ended generative design settings with  $10^4$ – $10^6$  candidates, the agent’s categorical reasoning about linkage stability is expected to provide even greater advantage, though this remains to be demonstrated. Fourth, the agent operates with sampling-with-replacement, tending to re-evaluate known hits rather than explore; deduplication strategies that preserve chemical reasoning remain an open challenge. Finally, the composite stability index  $S_{\text{CSI}}$  is a computational proxy that captures linkage chemistry, steric shielding, and hydrophobicity but does not account for the electronic influence of substituents proximal to the linkage bond on hydrolytic susceptibility, nor for framework crystallinity, both of which affect long-term durability under operating conditions. Experimental validation of hydrolytic stability under photocatalytic conditions is required to confirm the practical utility of the discovered candidates.

These findings open several avenues for future investigation. DFT validation of the top-ranked vinylene-linked candidates (TFP-OH1 + DVB + vinylene + tBu, reward 0.921; TFB + DVB + vinylene + OMe, reward 0.900) would establish whether the xTB-level predictions translate to accurate periodic band structures and band positions. Multi-model comparisons (Claude, GPT) would test whether the observed advantage reflects general LLM chemical priors or model-specific capabilities. Hybrid LLM–BO strategies could combine the agent’s rapid convergence with BO’s systematic exploration, potentially achieving both high sample efficiency and broad coverage. Multi-agent architectures, incorporating planner, critic, and memory components, may enable more sophisticated long-horizon reasoning. Expansion of the search space to include topology variation (honeycomb, kagome, square), pore-size engineering, and mixed-linker systems would test the agent’s reasoning in higher-dimensional design spaces. Finally, extension to other material classes, metal-organic frameworks, zeolites, and hybrid perovskites, would establish the generality of agent-guided inverse design.

## Methods

### COF search space definition

The candidate space comprised 820 COF building-block combinations generated from a curated library of seven trigonal ( $C_3$  symmetric) nodes, nineteen ditopic linkers, four linkage chemistries (imine,  $\beta$ -ketoenamine, hydrazone, vinylene), and ten aromatic R-group substituents (H, OH,  $\text{NH}_2$ , OMe, F,  $\text{CF}_3$ ,  $\text{NO}_2$ , Me, tBu,  $\text{SO}_3\text{H}$ ). Compatibility constraints reduced the combinatorial product. Imine linkages ( $\text{C}=\text{N}$ ) form by Schiff base condensation between aldehyde and primary amine functional groups; in our library, these arise from aldehyde nodes paired with diamine linkers, or amine nodes paired with dialdehyde linkers.  $\beta$ -Ketoenamine linkages require 1,3,5-triformylphloroglucinol-type aldehydes bearing enolisable  $\beta$ -diketone motifs paired with primary amines; here, only the Tp node satisfies this requirement, paired with diamine linkers. Hydrazone linkages form between aldehyde and hydrazide functional groups; in our library, aldehyde nodes are paired with dihydrazide linkers. Vinylene linkages ( $\text{C}=\text{C}$ ) form via Knoevenagel condensation between aldehydes and active methylene groups; in our library, aldehyde nodes are paired with DVB (1,4-bis(cyanomethyl)benzene).

The aldehyde nodes were TFB (1,3,5-triformylbenzene), TFPT-ald (triazine-2,4,6-tricarbaldehyde), TFP-OH1 (2-hydroxy-1,3,5-triformylbenzene), and Tp (1,3,5-triformylphloroglucinol); the amine

nodes were TAPB (1,3,5-tris(4-aminophenyl)benzene), TAPT (2,4,6-tris(4-aminophenyl)-1,3,5-triazine), and TAPA (tris(4-aminophenyl)amine). The breakdown by linkage type was: imine (aldehyde + diamine) 440, imine (amine + dialdehyde) 150,  $\beta$ -ketoenamine 110, hydrazone 80, and vinylene 40 candidates. Three node-linker combinations that consistently failed fragment assembly (TAPB + Thieno-DA, TAPT + OMe-PDA, TAPA + Thieno-DA) were retained in the enumeration but excluded from analysis when assembly failed.

## Fragment-based screening pipeline

Each candidate was evaluated through a fragment-based computational pipeline. First, a node-linker-node repeat-unit fragment was assembled from SMILES building blocks using RDKit [32] reaction SMARTS specific to each linkage chemistry: imine condensation (aldehyde + amine  $\rightarrow$  C=N),  $\beta$ -ketoenamine tautomerization (via Tp + amine), hydrazone formation (aldehyde + hydrazide), and Knoevenagel condensation (aldehyde + vinyl  $\rightarrow$  C=C). When the specified R-group was not hydrogen, SMARTS-based substitution replaced one aromatic hydrogen on the linker. The assembled fragment SMILES was converted to a three-dimensional structure via RDKit’s ETKDGV3 embedding with subsequent MMFF94 force-field minimization, yielding an initial geometry of typically 50–80 atoms.

Geometry optimization was performed with GFN1-xTB (version 6.7.1) [15] at the “tight” convergence level. The fundamental gap was computed via the vertical ionization potential and electron affinity protocol (`xtb --vipea`), which performs delta-SCF calculations on the optimised neutral geometry to obtain IP and EA values; the fundamental gap was taken as IP – EA. The linear transfer function (Eq. 1) was applied to map xTB fundamental gaps onto the DFT scale, calibrated against literature DFT band gaps for 13 COFs spanning six linkage types (including boronate ester, boroxine, and triazine linkages not present in the search space; Supplementary Table S2). The corrected gap was clipped to the range 0.5–6.0 eV to suppress unphysical outliers. The CBM position relative to NHE was estimated as

$$\text{CBM}_{\text{vs NHE}} = -\text{EA}_{\text{xTB}} + 2.62 \text{ V}, \quad (2)$$

where the offset was calibrated from three COFs with experimentally determined band-edge positions: TpPa-1, TAPB-PDA, and sp2c-COF [33, 34, 35]. The typical computational cost was 5–10 seconds per candidate for geometry optimization and vipea on a single CPU core.

## Composite stability index

To encode hydrolytic stability as a continuous, differentiable score, we defined a composite stability index  $S_{\text{CSI}}$  combining three components:

$$S_{\text{CSI}} = 0.50 S_{\text{linkage}} + 0.30 S_{\text{shielding}} + 0.20 S_{\text{hydrophobicity}}. \quad (3)$$

The linkage stability score  $S_{\text{linkage}}$  was assigned based on the well-established hydrolytic stability hierarchy of COF linkages [10, 36, 37, 38, 39]: imine 0.40, hydrazone 0.60,  $\beta$ -ketoenamine 0.80, and vinylene 0.95. This ordering reflects the underlying bond chemistry: imine C=N bonds undergo reversible hydrolysis; hydrazone linkages are moderately protected by the adjacent amide;  $\beta$ -ketoenamine bonds are stabilised by irreversible enol-keto tautomerization and intramolecular C=O  $\cdots$  H-N hydrogen bonding [36]; and vinylene C=C bonds are non-hydrolysable [39].

The steric shielding score  $S_{\text{shielding}}$  quantified the local protection of the linkage bond from nucleophilic attack by water. For each candidate, the atoms forming the linkage bond were identified

via SMARTS pattern matching on the fragment SMILES: [CH]=[N] for imine, [NH]-[CX3]=[OX1] (carbonyl C and O) for  $\beta$ -ketoenamine, [CH]=[N][NH] (C and first N) for hydrazone, and [CH]=[CH] for vinylene. The midpoint of these atoms in the xTB-optimised geometry served as the reference point, and  $S_{\text{shielding}}$  was computed as the number of heavy atoms within a 4 Å radius, normalised as  $\text{clip}((\text{count} - 5)/15, 0, 1)$ . When SMARTS matching failed (e.g., due to unusual valence states), the molecular centre of mass was used as a fallback.

The hydrophobicity score  $S_{\text{hydrophobicity}}$  was computed as the Crippen partition coefficient (SLogP) of the fragment SMILES using RDKit, normalised to the range [0, 1]. Higher hydrophobicity disfavours water access to the linkage bond, contributing to hydrolytic stability.

A sensitivity analysis across 30 weight triples ( $S_{\text{linkage}}$  weight from 0.3 to 0.7; remainder distributed between  $S_{\text{shielding}}$  and  $S_{\text{hydrophobicity}}$  in 0.1 increments) confirmed that the agent’s advantage over random search exceeded 2× for all weight combinations where the search space contained at least 10 hits (Supplementary Fig. S1).

## Hit criteria and reward function

A candidate was classified as a hit if it simultaneously satisfied three criteria: (1) corrected band gap between 1.8 and 2.2 eV, targeting the visible-light absorption window for photocatalytic water splitting; (2) CBM below 0 V versus NHE, the thermodynamic requirement for proton reduction; and (3)  $S_{\text{CSI}} \geq 0.7$ , ensuring adequate hydrolytic stability.

A continuous reward function was defined to guide the search methods:

$$r = 0.35 g_{\text{score}} + 0.30 \text{cbm}_{\text{score}} + 0.35 S_{\text{CSI}}, \quad (4)$$

where

$$g_{\text{score}} = \exp\left(-\frac{1}{2} \left(\frac{g - 2.0}{0.3}\right)^2\right), \quad (5)$$

$$\text{cbm}_{\text{score}} = \frac{1}{1 + \exp(5.0 \times \text{CBM}_{\text{vs NHE}})}. \quad (6)$$

The reward ranged from 0 to approximately 1, with values above 0.85 typically corresponding to hits.

## Search methods

Three search methods were compared, each evaluated over 200 iterations with five random seeds (42, 123, 456, 789, 2024) using a shared evaluation cache to ensure identical computational results for identical candidates.

**Random search.** Candidates were sampled uniformly at random (with replacement) from the 820-member candidate pool. This served as the null-hypothesis baseline.

**Bayesian optimization (BO).** A Gaussian process (GP) surrogate was fitted on 2048-bit Morgan fingerprints (radius 2) of assembled fragment SMILES, computed via RDKit. Features were standardized with a zero-mean, unit-variance scaler. The GP used a Matérn kernel ( $\nu = 2.5$ , length scale 1.0, bounds  $[10^{-3}, 100]$ ) with normalized targets, fitted with five random restarts of the L-BFGS-B optimizer [40]. The first 20 iterations used random initialization; subsequent

iterations selected the candidate with the highest expected improvement (EI) among unevaluated candidates. Evaluated candidates were tracked and excluded from subsequent acquisition-function maximization, ensuring that each iteration evaluated a novel candidate. This built-in deduplication is a standard feature of BO that contributes to its exploration efficiency. By contrast, the LLM agent operated with sampling-with-replacement, preserving its natural tendency to exploit high-reward chemical families; the trade-off between this exploitative behavior and exploration breadth is examined in the Discussion.

**LLM agent (Ara).** The agent used Google’s Gemini-3-flash-preview model [30] in JSON output mode (temperature 0.3, max 1024 output tokens). At each iteration, the agent received a prompt containing: (a) a system instruction describing the COF design task, available building blocks, compatibility constraints, and chemical principles (donor–acceptor theory, conjugation effects, stability–activity trade-off); (b) the results of the last 10 evaluations and the top 5 by reward from the full history; and (c) a request to select one (node, linker, linkage, R-group) combination with 1–3 sentences of chemical reasoning. The agent’s response was parsed for the four building-block identifiers; when parsing failed or the response was empty, a random candidate was substituted (contributing to the reported parse-failure rate). No explicit deduplication was enforced: the agent was free to re-evaluate previously selected candidates, relying on the soft guidance in the prompt (“choose a NEW combination you have not tried before if possible”) and the list of previously evaluated candidates to encourage diversity. The consequences of this sampling-with-replacement design for exploration diversity are examined through oracle recovery analysis in the Discussion.

**Statistical testing.** Pairwise comparisons of cumulative hits across seeds were performed using the one-sided Mann–Whitney  $U$  test, with significance declared at  $p < 0.05$ .

## Ground-truth evaluation

To establish a ground-truth benchmark, all 820 candidates in the search space were submitted to the fragment-based screening pipeline. Of these, 670 (81.7%) were successfully evaluated; the remaining 150 failed at fragment assembly or xTB convergence. Among the 670 evaluated candidates, 38 satisfied all three hit criteria (Supplementary Table S3), yielding a global hit rate of 5.7%. Oracle recovery was defined as the fraction of these 38 ground-truth hits discovered at least once (unique hits only, with no double-counting of repeated evaluations) within a method’s 200-iteration budget.

**Reasoning trace collection.** To obtain interpretable reasoning examples (Table 2), a separate 20-iteration run was performed using the same model (Gemini-3-flash-preview) and system prompt, with the maximum output-token limit increased from 1024 to 4096 to avoid truncation of reasoning text and the temperature raised to 0.5 to encourage more diverse reasoning. All other generation parameters (JSON output mode, safety settings) were unchanged. This run was used for qualitative analysis only and did not contribute to the quantitative comparison.

## Data availability

Data supporting the findings of this study are available in the following locations:

- **Building blocks library** (nodes, linkers, linkages, R-groups): included in this repository as ‘data/building\_blocks\_library.json‘.
- **Calibration dataset** (xTB vs DFT band gaps for 13 COFs): ‘data/calibration\_dataset.csv‘.
- **CBM calibration** (conduction-band minimum vs NHE): ‘data/cbm\_calibration.json‘.
- **Comparative study outputs** (run results, oracle summary, full evaluation)

All other data generated or analysed during this study are either included in this repository or can be reproduced using the provided code and the above data files.

## Code availability

The code that supports the findings of this study is available at <https://github.com/Iman-Peivaste/Ara>. The repository includes the fragment-based screening pipeline (main entry point ‘main.py‘), search methods (random, Bayesian optimisation, and LLM agent), calibration and analysis scripts, and the building blocks library and calibration datasets required to reproduce the results. The pipeline relies on the GFN1-xTB implementation in the xtb programme (see Methods), RDKit for molecular handling, and (for COF construction) the Supramolecular ToolKit (stk). Instructions for environment setup and reproduction of the comparative study and figures are provided in the repository README.

## Author Contributions

Iman Peivaste: Conceptualization, developing the initial concept and workflow, framework design, writing the original draft, visualization, methodology, investigation, and formal analysis.

Nicolas Boscher: Writing, review, editing, resources, methodology, and formal analysis.

Ahmed Makradi: Writing, review, editing, methodology, and formal analysis.

Salim Belouettar: Supervision, funding acquisition, conceptualization (research direction and framing), writing – review & editing, methodology, resources.

## Competing Interests

The authors declare that they have no known competing financial interests or personal relationships that could have appeared to influence the work reported in this paper.

## Acknowledgements

This work was funded by the Luxembourg Fonds National de la Recherche (FNR) through the grant PRIDE21/16758661/HYMAT.

## References

- [1] Chen, S., Takata, T. & Domen, K. Particulate photocatalysts for overall water splitting. *Nature Reviews Materials* **2**, 17050 (2017).
- [2] Wang, Q. & Domen, K. Particulate photocatalysts for light-driven water splitting: mechanisms, challenges, and design strategies. *Chemical Reviews* **120**, 919–985 (2019).
- [3] Tao, X., Zhao, Y., Wang, S., Li, C. & Li, R. Recent advances and perspectives for solar-driven water splitting using particulate photocatalysts. *Chemical Society Reviews* **51**, 3561–3608 (2022).
- [4] Qi, J., Zhang, W. & Cao, R. Solar-to-hydrogen energy conversion based on water splitting. *Advanced Energy Materials* **8**, 1701620 (2018).
- [5] Ding, S.-Y. & Wang, W. Covalent organic frameworks (cofs): from design to applications. *Chemical Society Reviews* **42**, 548–568 (2013).
- [6] Côté, A. P. *et al.* Porous, crystalline, covalent organic frameworks. *science* **310**, 1166–1170 (2005).
- [7] Geng, K. *et al.* Covalent organic frameworks: design, synthesis, and functions. *Chemical reviews* **120**, 8814–8933 (2020).
- [8] Stegbauer, L., Schwinghammer, K. & Lotsch, B. V. A hydrazone-based covalent organic framework for photocatalytic hydrogen production. *Chemical Science* **5**, 2789–2793 (2014).
- [9] Vyas, V. S. *et al.* A tunable azine covalent organic framework platform for visible light-induced hydrogen generation. *Nature communications* **6**, 8508 (2015).
- [10] Lyu, H., Diercks, C. S., Zhu, C. & Yaghi, O. M. Porous crystalline olefin-linked covalent organic frameworks. *Journal of the American Chemical Society* **141**, 6848–6852 (2019).
- [11] Xu, H., Gao, J. & Jiang, D. Stable, crystalline, porous, covalent organic frameworks as a platform for chiral organocatalysts. *Nature chemistry* **7**, 905–912 (2015).
- [12] Ongari, D., Yakutovich, A. V., Talirz, L. & Smit, B. Building a consistent and reproducible database for adsorption evaluation in covalent–organic frameworks. *ACS central science* **5**, 1663–1675 (2019).
- [13] Haase, F. & Lotsch, B. V. Solving the cof trilemma: towards crystalline, stable and functional covalent organic frameworks. *Chemical Society Reviews* **49**, 8469–8500 (2020).
- [14] Jain, A., Shin, Y. & Persson, K. A. Computational predictions of energy materials using density functional theory. *Nature Reviews Materials* **1**, 1–13 (2016).
- [15] Grimme, S., Bannwarth, C. & Shushkov, P. A robust and accurate tight-binding quantum chemical method for structures, vibrational frequencies, and noncovalent interactions of large molecular systems parametrized for all spd-block elements ( $z= 1-86$ ). *Journal of chemical theory and computation* **13**, 1989–2009 (2017).
- [16] Hachmann, J. *et al.* The harvard clean energy project: large-scale computational screening and design of organic photovoltaics on the world community grid. *The Journal of Physical Chemistry Letters* **2**, 2241–2251 (2011).

- [17] Shields, B. J. *et al.* Bayesian reaction optimization as a tool for chemical synthesis. *Nature* **590**, 89–96 (2021).
- [18] Griffiths, R.-R. & Hernández-Lobato, J. M. Constrained bayesian optimization for automatic chemical design using variational autoencoders. *Chemical science* **11**, 577–586 (2020).
- [19] Butler, K. T., Davies, D. W., Cartwright, H., Isayev, O. & Walsh, A. Machine learning for molecular and materials science. *Nature* **559**, 547–555 (2018).
- [20] Moosavi, S. M., Jablonka, K. M. & Smit, B. The role of machine learning in the understanding and design of materials. *Journal of the American Chemical Society* **142**, 20273–20287 (2020).
- [21] Peivaste, I. *et al.* Artificial intelligence in materials science and engineering: Current landscape, key challenges, and future trajectories. *Composite Structures* **372**, 119419 (2025).
- [22] Peivaste, I., Makradi, A., Mercuri, F. & Belouettar, S. Hype-mad: high-yield python environment for molecular automation and data generation. *Acta Mechanica* 1–9 (2025).
- [23] Jablonka, K. M., Schwaller, P., Ortega-Guerrero, A. & Smit, B. Leveraging large language models for predictive chemistry. *Nature Machine Intelligence* **6**, 161–169 (2024).
- [24] Zheng, Z., Zhang, O., Borgs, C., Chayes, J. T. & Yaghi, O. M. Chatgpt chemistry assistant for text mining and the prediction of mof synthesis. *Journal of the American Chemical Society* **145**, 18048–18062 (2023).
- [25] Boiko, D. A., MacKnight, R., Kline, B. & Gomes, G. Autonomous chemical research with large language models. *Nature* **624**, 570–578 (2023).
- [26] Schwaller, P. *et al.* Molecular transformer: a model for uncertainty-calibrated chemical reaction prediction. *ACS central science* **5**, 1572–1583 (2019).
- [27] Ramos, M. C., Michtavy, S. S., Porosoff, M. D. & White, A. D. Bayesian optimization of catalysts with in-context learning. *arXiv preprint arXiv:2304.05341* (2023).
- [28] Peivaste, I., Makradi, A. & Belouettar, S. Chemnavigator: Agentic ai discovery of design rules for organic photocatalysts. *arXiv preprint arXiv:2601.17084* (2026).
- [29] M. Bran, A. *et al.* Augmenting large language models with chemistry tools. *Nature machine intelligence* **6**, 525–535 (2024).
- [30] Team, G. *et al.* Gemini: a family of highly capable multimodal models. *arXiv preprint arXiv:2312.11805* (2023).
- [31] Onida, G., Reining, L. & Rubio, A. Electronic excitations: density-functional versus many-body green’s-function approaches. *Reviews of modern physics* **74**, 601 (2002).
- [32] Rdkit: Open-source cheminformatics. <https://www.rdkit.org>. Accessed: 2026-02-17.
- [33] Bi, S. *et al.* Two-dimensional semiconducting covalent organic frameworks via condensation at arylmethyl carbon atoms. *Nature Communications* **10**, 2467 (2019).
- [34] Wang, X. *et al.* Sulfone-containing covalent organic frameworks for photocatalytic hydrogen evolution from water. *Nature Chemistry* **10**, 1180–1189 (2018).
- [35] Wei, S. *et al.* Semiconducting 2d triazine-cored covalent organic frameworks with unsubstituted olefin linkages. *Journal of the American Chemical Society* **141**, 14272–14279 (2019).

- [36] Kandambeth, S. *et al.* Construction of crystalline 2d covalent organic frameworks with remarkable chemical (acid/base) stability via a combined reversible and irreversible route. *Journal of the American Chemical Society* **134**, 19524–19527 (2012). URL <https://doi.org/10.1021/ja308278w>.
- [37] Banerjee, R. *et al.* Chemically stable multilayered covalent organic nanosheets from covalent organic frameworks via mechanical delamination. *Journal of the American Chemical Society* **135**, 17853–17861 (2013). URL <https://doi.org/10.1021/ja408121p>.
- [38] DeBlase, C. R. & Dichtel, W. R. Moving beyond boron: The emergence of new linkage chemistries in covalent organic frameworks. *Macromolecules* **49**, 5297–5305 (2016). URL <https://doi.org/10.1021/acs.macromol.6b00891>.
- [39] Zhuang, X. *et al.* A two-dimensional conjugated polymer framework with fully sp<sup>2</sup>-bonded carbon skeleton. *Polymer Chemistry* **7**, 4176–4181 (2016). URL <https://doi.org/10.1039/C6PY00561F>.
- [40] Byrd, R. H., Lu, P., Nocedal, J. & Zhu, C. A limited memory algorithm for bound constrained optimization. *SIAM Journal on Scientific Computing* **16**, 1190–1208 (1995). URL <https://doi.org/10.1137/0916069>.